Atmos. Meas. Tech. Discuss., 6, 9579–9621, 2013
www.atmos-meas-tech-discuss.net/6/9579/2013/
doi:10.5194/amtd-6-9579-2013

Atmospheric Measurement Techniques Discussions

Evaluation of gridded Scanning ARM Cloud Radar reflectivity observations and vertical Doppler velocity retrievals

K. Lamer, A. Tatarevic, I. Jo, and P. Kollias

Department of Atmospheric and Oceanic Sciences McGill University, Montreal, Canada

Received: 20 August 2013 – Accepted: 25 October 2013 – Published: 8 November 2013

Correspondence to: K. Lamer (katia.lamer@mail.mcgill.ca)

Published by Copernicus Publications on behalf of the European Geosciences Union.

Abstract

The Scanning ARM Cloud Radars (SACR's) provide continuous atmospheric observations aspiring to capture the 3-D cloud-scale structure. Sampling clouds in 3-D is challenging due to their temporal-spatial scales, the need to sample the sky at high elevations and cloud radar limitations. Thus, a common scan strategy is to repetitively slice the atmosphere from horizon to horizon as clouds advect over the radar (Cross-Wind Range Height Indicator – CWRHI). Here, the processing and gridding of the SACR CW-RHI scans are presented. First, the SACR sample observations from the ARM Oklahoma (SGP) and Cape-Cod (PVC) sites are post-processed (detection mask, velocity de-aliasing and gaseous attenuation correction). The resulting radial Doppler moment fields are then mapped to Cartesian coordinates with time as one of the dimension. The Cartesian-gridded Doppler velocity fields are next decomposed into the horizontal wind velocity contribution and the vertical Doppler velocity component. For validation purposes, all gridded and retrieved fields are compared to collocated zenith pointing ARM cloud radar measurements. We consider that the SACR sensitivity loss with range, the cloud type observed and the research purpose should be considered in determining the gridded domain size. Our results also demonstrate that the gridded SACR observations resolve the main features of low and high stratiform clouds. It is established that the CW-RHI observations complemented with processing techniques could lead to robust 3-D clouds dynamical representations up to 25–30 ° off zenith. The proposed gridded products are expected to advance our understanding of 3-D cloud morphology, dynamics, anisotropy and lead to more realistic 3-D radiative transfer calculations.

1 Introduction

Ground-based and space-borne cloud radars are the primary instruments used to resolve clouds' vertical structure as well as their dynamical and microphysical proper-

AMTD
6, 9579–9621, 2013

ties. Through ongoing research and development over the last two decades, millimeter wavelength radar sophistication and availability in different atmospheric research platforms has significantly increased (Kollias et al., 2007). During this period, the bulk of the cloud radar observations were collected in a zenith-pointing mode (profiling). Undeniably, scientists and modelers have cleverly used vertical-column radar information complemented with lidar and radiometer information to improve our knowledge of clouds (Shupe et al., 2011; Rémillard et al., 2012) as well as their parameterization in cloud models of variable scales ranging from Large Eddy Simulations to Global Climate Models (Randall et al., 1996; Somerville and Iacobellis 1999; Qian et al., 2012). However, the lack of factual 3-D cloud structure information hinders our ability to quantify the 3-D radiative effects, measure the cloud field anisotropy and introduces uncertainty in cloud properties retrievals (Hinkelman et al., 2005; Davis et al., 1997; Zinner and Mayer, 2006).

Continual advancements in millimeter wavelength radar technology permitted the deployment of a number of scanning cloud radars (Mather and Voyles, 2013) that can operate off-zenith, thus providing a hemispheric view of the cloudy atmosphere. Scanning radars are not new and have been widely used by the weather community in forecasting and research applications. However, weather radars and cloud radars have different coverage objectives (large distances vs. cone of silence), antenna scan rates (much lower for cloud radars due to their narrow beam width) and targets with different temporal-spatial characteristics (Kollias et al., 2013a). Weather radars mostly use volume coverage patterns designed to provide large horizontal coverage at low-levels using a sequence of constant elevation PPI (Plain Position Indicator) scans. On the contrary, scanning cloud radars need to sample the part of the atmosphere near and above the ground-based facility, and thus, deploy innovative scanning strategies such as the cross wind scan strategy. This scanning strategy relies on a sequence of constant azimuth RHI (range height indicator) scans with changing elevation (0–180°) to slice the cloudy atmosphere as it advects over the radar (CW-RHI, Kollias et al., 2013a). Using a sequence of these scans, with time as one of the dimensions, we

AMTD
6, 9579–9621, 2013

can interpolate to a Cartesian grid the 3-D morphological (reflectivity) and dynamical (Doppler velocity) cloud structure. Gridded scanning cloud radar observations would provide complete information on cloud overlap conditions, as well as allow a new view to cloud life-cycle analysis. They could also tighten constraints on radiative transfer calculations. In addition, cloud 3-D dynamical representation can be used to characterize cloud-scale turbulence including the vertical and horizontal organization of large-eddies, their extent, tilt, and orientation with respect to the mean flow and large-scale meteorology.

Here, CW-RHI and collocated profiling cloud radars observations are used to evaluate (i) the reconstruction of the 3-D radar reflectivity and Doppler velocity fields and (ii) the retrieval of the 3-D vertical Doppler velocity field after the removal of the horizontal wind contribution. It is established that the CW-gridding does not alter the data and facilitates interpretation. It is also determined that the reduction of radar sensitivity with range should be one of the factors determining the grid space size. Moreover, the proposed decomposition technique to retrieve radar plane wind contribution resulted in a range of confident vertical velocity retrievals extending to 25–30°.

The observational settings, the radar characteristics, scan strategy and raw data post-processing are described in Sect. 2. The Cartesian CW-gridding algorithm is described and evaluated in Sect. 3. Section 4 contains the description and evaluation of a technique to isolate vertical Doppler velocity from observed radial Doppler velocity. Summary and recommendations are provided in the last section.

2 Observation and raw data post-processing

The US Department of Energy created the ARM program in the mid 90 s aiming, among else, to increase our understanding of the effect of clouds on radiative fluxes and accordingly to improve our modeling capabilities (Stokes and Schwartz, 1994). Currently, the ARM program deploys multiple fixed and mobile facilities designed to observe various cloud types and connect cloud-scale processes and properties to the large-scale

AMTD
6, 9579–9621, 2013

meteorology (Mather and Voyles, 2013). The large array of collocated instruments on site provides a unique opportunity to examine agreements in observational techniques among instruments, as well as to evaluate the accuracy of different methodologies applied to measurements.

This study's dataset was obtained at two sites. First, the ARM Mobile Facility in Cape Cod, MA (PVC) during the Two-Column Aerosol Project (TCAP) field campaign, which took place in summer 2012 for a period of 12 months and aimed at quantifying aerosol properties, radiation and cloud characteristics. The case study presented here is from 19 November 2012. The site's proximity to the coast limited land contamination and enabled marine stratocumulus observations. Second, the Southern Great Plains (SGP), OK, an ARM fixed site, which is characterized by a relatively homogeneous geography and a wide variability of atmospheric conditions and cloud types. The case study presented here is from 07 December 2012.

The data of this study was obtained with the Ka-band (35.3 GHz) SACR a fully coherent dual-frequency, dual-polarization Doppler radar mounted on a common scanning pedestal paired with either a W-band (94.0 GHz) or an X-band (9.7 GHz) radar depending on the location of deployment (Fig. 1a) (only data from the Ka-band radar was used for this study). The specific settings of the instruments for each site are provided in Table 1. The radar operated the Cross-Wind Range Height Indicator (CW-RHI) scan strategy, which consists of operating multiple horizon-to-horizon scans at an azimuth perpendicular to the leading wind directions (Cape Cod 225° and SGP 180°) for a chosen time period (Fig. 1b). In the presented cases, the scans were repeated during 19 min to form a total of 60 blocks of horizon-to-horizon observations. An average of 20 sets of nineteen-minute duration were collected per day.

Both sites were also equipped with collocated profiling cloud radars: the W-band (95 GHz) ARM Cloud Radar (WACR) at Cape Cod and the Ka-band ARM Zenith-pointing Radar (KAZR) at the SGP. Those zenith-pointing Doppler radars collected continuous data over the period of the field experiments. Although providing a very

AMTD
6, 9579–9621, 2013

good temporal coverage, their view was limited to 2-D time-height information. More specific information about these instruments is also provided in Table 1.

Finally sounding information was collected with a radiosonde 4 times per day approximately at 05:30, 11:30, 17:30, and 23:30 UTC.

The first step in SACR data post-processing is the identification of radar volumes containing atmospheric returns (clouds, insects and ground clutter). At each radar profile, the receiver noise is identified and a preliminary binary feature mask is estimated using a power threshold. Using a range-elevation spatial filter, a refined feature mask is estimated (Clothiaux et al., 1995; Hildebrand and Sekhon, 1974)

Second, the nearest (in time) atmospheric sounding is used to extract the profiles of water vapor, pressure and temperature, which, along with standard atmospheric O_2 and N_2 concentrations, are projected on the SACR slant line-of-sight. The projected profiles are used as input to the Rosenkranz (1998) line-by-line absorption model to estimate the two-way gaseous attenuation along all SACR beam paths used to correct reflectivity observations.

The next step in the Ka-SACR data post-processing is the application of an insect filter to remove non-meteorological returns in the boundary layer. The insect filter is applied to profiles where cloud bases are detected within a one-hour window and heights where the temperature is higher than 5 °C. Where these conditions are satisfied, the algorithm uses the linear depolarization ratio measurements to distinguish insect returns from clouds.

Finally, the SACR radial Doppler velocities are unfolded. The nearest atmospheric soundings' wind velocity magnitude and direction serve as an estimate of the actual radial velocities on the radar plane. This estimate is then compared to the radar velocity observations and Nyquist velocity to make a first guess of the number of foldings which is then refined using a cost-function that ensures smoothness across range. A detailed methodology of the quality-control processing of the SACR observations can be found in Kollias et al. (2013b).

AMTD
6, 9579–9621, 2013

3 Gridding

The post-processed CW-RHI SACR radar observables (Sect. 2) are used as inputs to the CW-gridding algorithm described here.

3.1 Radar sensitivity

A challenge closely related to the quality of gridded data is radar sensitivity. In weather radars, the key challenges in interpreting long-range observations are related to Earth's curvature and the broadening of the radar beam. The drop in radar sensitivity with the square of the distance from the radar is not a major concern since weather radars operational mandate is related to the detection of intense echoes from severe weather. For the Ka-SACR, large sampling volumes and long ranges are not an issue since the radar has a very narrow beamwidth (0.33°) and typically operates within a range of 20 km. Given that one of the main operational mandates of the Ka-SACR is to provide detailed characterization of hydrometeor locations in 3-D and since the radar-lidar instrument synergy for the determination of hydrometeor layers is not possible (Clothiaux et al., 2000), the determination of the cloud locations is based on Ka-SACR observations only. Thus, the drop of the radar sensitivity with the square of the distance from the radar can lead to significant range-depended biases when it comes to fundamental cloud properties such as cloud fraction and cloud boundaries.

The impact of reduced sensitivity with range on cloud fraction is shown in Fig. 2. All stratocumulus clouds (a total of 600 h) observed by the WACR (Table 1) during the Cloud, Aerosol and Precipitation in the Marine Boundary Layer (CAP-MBL) field experiment (Rémillard et al., 2012) are used in this figure. The marine stratocumulus observations are separated into two classes: non-drizzling periods, when the radar-detected hydrometeor base is less than 100 m below the ceilometer detected cloud base and drizzling periods otherwise. For each class and each-hour of observations, the radar-derived hourly cloud fraction is estimated for different levels of radar sensitivity. It is clear that radar sensitivity plays a critical role in the observed cloud fractions.

AMTD
6, 9579–9621, 2013

For a radar sensitivity of −40 dBZ or better most stratocumulus clouds are detected (cloud fraction near 100 %). As the radar sensitivity is degraded (from −40 to −20 dBZ), there is a very rapid change in the measured cloud fraction (∼ 8 % per 1 dBZ drop in sensitivity). Almost all clouds are not detected for radar sensitivity lower than −20 dBZ. Drizzling clouds have higher reflectivities and thus, their cloud fraction is more resilient to changes in radar sensitivity. Similar plots can be constructed at all ARM sites. At the ARM SGP, shallow cumuli represent an even more challenging target to detect and at the ARM NSA site, the presence of highly reflecting ice particles for most of the year to lesser dependency to the radar sensitivity. For reference, the Ka-SACR has an estimated sensitivity of −50 dBZ at 1 km (−30 dBZ at 10 km) during nominal operational setting.

3.2 Radar interpolation schemes

For weather radars, the volumetric radar observations collected in five minutes are considered instantaneous. Commonly used schemes for gridding such observations to 3-D Cartesian space are the distance depended weighted-averaging schemes based on Cressman (1959) and Barnes (1964) weighting functions (Askelson, 1996). Other applied schemes are those based on the nearest neighbor method (Jorgensen et al., 1983) and on bilinear interpolation (Mohr and Vaughan, 1979; Miller et al., 1986; Fulton, 1998). Trapp and Doswell III (2000) analyzed the various theoretical aspects of these schemes and recommended that both the choice of interpolation scheme and the choice of weighting function parameters should be problem specific. They showed that the root-mean-square (rms) differences are smaller in the case of "adaptive" (weighting function defined relative to grid spacing) rather than in the case of "traditional" Cressman and Barnes methods (fixed weighting function parameters). The "traditional" Barnes and Cressman methods perform the best in preserving both amplitude and phase of observables, while the errors in amplitude in "adaptive" methods increase with increasing range and data point spacing. Bilinear and nearest neighbor methods generate noise due to smaller-scale wavelengths not present in the initial field and are

AMTD
6, 9579–9621, 2013

inferior to the interpolation methods mentioned above, although rms errors between the analyses and observations are the smallest. Zhang, Howard and Gourley (2005) evaluated several gridding methods in order to find the best interpolation approach that retains physical characteristics of raw reflectivity with minimum smoothing or introduction of artifacts on high spatial ($\leq$ 1 km) and temporal resolution ($\leq$ 5 min) for real-time applications. The analyzed methods are: radar beam volume mapping (a grid cell is considered to be within a radar bin if the center of the grid cell is contained inside the volume of the radar bin), nearest neighbor method, vertical interpolation method, and horizontal and vertical interpolation method. They found that the most suitable method is a scheme combining a nearest-neighbor mapping on the range and azimuth plane and a linear interpolation in the elevation direction. Also, a vertical interpolation is preferred for analyses of convective-type echoes, while vertical and horizontal interpolations are recommended for analyses of stratiform echoes.

3.3 CW-gridding algorithm

The gridding of Ka-SACR CW-RHI observations is subject to three important facts: the time duration and geometry of the scans as well as the space-time overlap between scans. The elevation scan rate of the Ka-SACR is set to 9° per second; thus, it takes about 20 s to complete a horizon-to-horizon CW-RHI scan. A sequence of 60 such 2-D scans represents a complete set of CW-RHI Ka-SACR (Fig. 1b). The Ka-SACR beamwidth is 0.33° and the radar performs signal integration and records a profile of radar observables every 0.33° of elevation change, thus, it provides a complete coverage with no gaps in the range-height plane. The Ka-SACR produces 26–27 range-resolved measurements of 30 m resolution (Table 1).

3.3.1 2-D-gridding algorithm

The polar coordinate Ka-SACR observations are first gridded in a height-along scan distance 2-D Cartesian grid and are then interpolated in time. At 100 m range from

AMTD
6, 9579–9621, 2013

the Ka-SACR, the shortest distance between centers of radar resolution volume at two adjacent elevations (the chord length) is 0.5 m while at 15 km range is 80 m. Thus, at short range, the radar observations in a contiguous set of elevations will influence more the values in a particular grid point, while at far range the radar observations along range will have a stronger weight on grid point value. The degree of smoothing effects depends on the chosen resolution in Cartesian space. The chosen gridding method thus has to be based on adaptive weights depending on both the size of the radar volume (in order to minimize the smoothing) and resolution in Cartesian space.

The polar (r, φ, θ) to Cartesian (x, y, z) transformation is performed for each individual observed cloud pixel. The standard atmospheric beam propagation model (Doviak and Zrnić, 1993) is assumed in all computations:

$$a_{\mathrm{ef}} = \frac{4}{3}a \tag{1}$$

$$z = \left(r^2 + a_{\mathrm{ef}}^2 + 2ra_{\mathrm{ef}}\sin\theta\right)^{0.5} - a_{\mathrm{ef}} \tag{2}$$

$$s = a_{\mathrm{ef}}\sin^{-1}\left(\frac{r\cos\theta}{a_{\mathrm{ef}} + z}\right). \tag{3}$$

where a represents the earth's radius, a_{ef} represents the 4/3-effective earth radius, z is the height of the center of the radar resolution volume, and s is the distance between the radar and the projection of the bin along the earth surface. The radar coordinates (r, φ, θ) represent the slant range, azimuth angle from east in our convention, and elevation angle from the horizon, respectively. Horizontal Cartesian coordinates x and y are then determined by:

$$x = s\cos\varphi \tag{4}$$

$$y = s\sin\varphi. \tag{5}$$

Setting the azimuth angle to zero degrees performs transition from 3-D to the range-height plane imposed by the CW scanning strategy. The effects of earth curvature are

AMTD
6, 9579–9621, 2013

included in the coordinate transformation equations although the target-plane approximation is appropriate for practical applications of CW–RHI radar data.

The Ka-SACR sampling strategy is such that the angle difference between two successive elevations is equal to the antenna 3-dB beamwidth, $\theta_{3\,\mathrm{dB}}$. In reality, and due to reasons associated with small fluctuation on the scanner rotational velocity and the real-processing computer efficiency, the angle difference between two successive elevations may differ from $\theta_{3\,\mathrm{dB}}$ so that somewhat small gaps between the adjacent elevations may exist. Analysis of a large volume of Ka-SACR observations indicated that typically the angle is seldom wider than two times the $\theta_{3\,\mathrm{dB}}$. For simplicity reasons, the antenna beamwidth in azimuthal direction is not taken into account in further discussion.

Radar observations centered at polar coordinate r_i, θ_j are considered to be representative of the area defined by range r_i, $\theta_{3\,\mathrm{dB}}$, and pulse length dr with polar coordinates $[P_1 = (r_i - \mathrm{d}r/2, \theta_i - \theta_{3\,\mathrm{dB}}/2)$, $P_2 = (r_i - \mathrm{d}r/2, \theta_i + \theta_{3\,\mathrm{dB}}/2)$, $P_3 = (r_i + \mathrm{d}r/2, \theta_i - \theta_{3\,\mathrm{dB}}/2)$, $P_4 = (r_i + \mathrm{d}r/2, \theta_i + \theta_{3\,\mathrm{dB}}/2)]$. The corresponding Cartesian coordinates of the radar resolution volume are computed and the smaller rectangle defined on the Cartesian grid that includes the radar resolution area is defined (Fig. 3). The algorithm estimates the polar coordinates for all grid points in the rectangle, and only those grid pixels inside of radar volume r_i, θ_j, (bounded by polar coordinates P_{1-4}) are considered to have a value influenced by observational value r_i, θ_{j},. Each grid point is allowed to "have a memory" of all "influencing" observational points and their distance from the grid point. In small distance from radar, the radar volume is very small compared to grid cell and it may not contain any grid point. In those cases, the value r_i, θ_j is considered to influence those grid points located in area at grid resolution distance from r_i, θ_j. Finally, once each radar resolution volume is examined, and the observational values that influence each specific grid point are identified, one of the following gridding methods is applied to estimate the radar value at the grid point: Maximum value, Mean value, Cressman and Barnes (see Appendix A for details on the available gridding methods).

AMTD
6, 9579–9621, 2013

3.3.2 Along-time gridding algorithm

Once the Ka-SACR polar coordinates observations are gridded in 2-D range-height planes, the gridded planes are interpolated in time (Fig. 4). The selected temporal resolution Δt is preferred to be greater than or equal to the average time between two successive scans (about 1 s for the Ka-SACR CW-RHI scans). Furthermore, Δt should not be higher than a quarter of the scan duration. A schematic of the scanning space at constant height z along the time dimension is shown in Fig. 4. The dashed lines represent few consecutive scans along the scanning direction x that appear tilted in time since each horizon-to-horizon scan required a finite time period to be completed (20 s). The grid resolution along the cross-wind direction as well as the temporal resolution (density of grid points along the time dimension) is user depended. First, using nearest neighbor method only along the time dimension, grids points are populated with the 2-D gridded values. The locations of those (x_{ev}, z, t_{ev}) points are denoted by the circles near the dashed lines in Fig. 4 and represent our best estimates of the gridded CW-RHI scanning radar observations, denoted by the expression "measured values" in further text.

The "measured values" are not regularly distributed along the time coordinate for different fixed positions at the scanning direction (x-axis). The time distance between the measured points varies between the average time between two successive scans and twice the time duration of the scan. For example, at the center of grid ($x = 0$), the distance between any two measured points is approximately 21 s, while at the furthest edges of x it varies between 1 and 41 s. The number of the regular time grid points Nt_{int} between any two measured values thus varies in function of grid resolution in time direction and properties of scanning technique. The values at these points are obtained using the two closest measured values at (x_{ev}, z_{ev}), the one from precedent and the one from succeeding scan. If the two measured values contain radar detections (case 1, Fig. 4), then linear interpolation is performed for all the Nt_{int} points between the two measured values. If one of the two measured values contains no radar detection (case

AMTD
6, 9579–9621, 2013

2, Fig. 4), then each measured value is assumed constant and propagated in half of the Nt_{int} points, thus, only to the start-time of the following and/or the end-time of the preceding scan.

3.3.3 Evaluation of the gridded SACR radar observables

A cirrus cloud sampled by the SGP Ka-SACR is used as an example to investigate the performance of the 2-D gridding algorithm and the influence of the selected interpolation scheme on the gridded radar reflectivity values (Fig. 5). The cirrus cloud is clearly detected over a 40 km range and has a double layer structure with cloud base at 7–8 km and cloud top at 10–11 km as mapped by the polar coordinates Ka-SACR post-processed data (Fig. 5a). The 2-D Cartesian gridded (Δx = 50 m, Δz = 50 m) field of Ka-SACR reflectivities using the Barnes scheme is a bit smoother as expected but all important features and scales of variability preserved (Fig. 5b). The 2-D gridded radar reflectivity differences of the Barnes scheme with the Cressman, the mean value and the maximum value interpolation schemes are shown in Fig. 5c–e. Very small differences are observed between the Barnes and the Cressman and mean interpolation schemes. The maximum value interpolation scheme results to higher overall reflectivity values compared to Barnes and subsequently compared to the Cressman and mean value schemes. Near the cirrus cloud edges and in areas with low radar reflectivity values (at ranges 15–20 km), the differences between the maximum value scheme and the Barnes are smaller. Their larger similarity in those areas is due to a lack of reflectivity variability due to lower radar sensitivity.

Another method to evaluate the performance of the various interpolation schemes consists in comparing the area distribution histograms of Ka-SACR reflectivities before and after gridding using all available interpolation schemes (Fig. 6). This is done for two cases, a cirrus cloud observed at the SGP and a stratus cloud observed at TCAP. The stratus cloud is characterized by lower radar reflectivities with a distribution peak at −42 dBZ (Fig. 6a). Due to its very low radar reflectivities the stratus cloud is not detected at ranges longer than 5 km from the Ka-SACR. The cirrus cloud is character-

AMTD
6, 9579–9621, 2013

ized by higher radar reflectivities with a distribution peak at −25 dBZ (Fig. 6b) and it is detected at ranges up to 20 km (Fig. 5a). Not surprising, the maximum value interpolation scheme shifts the area distribution histogram of reflectivities to higher values by 3 dB compared to before gridding. Furthermore, the area distribution histograms of the Cressman, Barnes and mean value interpolation schemes are very similar in both cases. Overall, there is reasonable agreement between the histograms of the three interpolation schemes and the Ka-SACR post-processed data. However, it is noticeable that in the case of the stratus cloud, the interpolation schemes produce a small bump (increase) in the areal coverage of lower reflectivities. This is imputable to the weak radar reflectivities of the non-precipitating stratus cloud that results in areal gaps near cloud edges that are filled with low radar reflectivity values during gridding. In the case of the cirrus cloud, a small increase in the areal coverage of low radar reflectivities is also observed but it is much smaller due to the relatively insignificant areal coverage of cloud edges compared to the thick and horizontally extensive cirrus area. On the other hand, the interpolation schemes produce a small bump in the areal coverage of high reflectivities, which can be attributed to the smoothing effect of the interpolation schemes (Fig. 6b).

An example of along-time gridding at constant height of 7175 m near the base of a cirrus cloud observed at the ARM SGP site is shown in Fig. 7. The location and density of the measured values are shown in the 2-D cloud mask (black areas in Fig. 7a). The location of the interpolated points (i.e., cloud pixels located between measured values located at preceding and succeeding scans) is shown (blue areas in Fig. 7a). Finally, the location of the propagated points (i.e., cloud pixels located between one missing and one present measured value) is shown (red areas in Fig. 7a). The corresponding Ka-SACR gridded reflectivity field is shown in Fig. 7b.

The observations from the collocated dedicated ARM profiling radars produce continuous high-resolution time-height observations and a method to: (i) evaluate the performance of the along-time gridding algorithm and (ii) investigate if the temporal spacing between the CW-RHI scans (currently 20 s over the radar location) is sufficient to

AMTD
6, 9579–9621, 2013

adequately capture cloud-scale variability. A comparison between the observed (post-processed), the gridded Ka-SACR extracted at zenith and the high-resolution KAZR observations is shown in Fig. 8. The comparison is limited to the radar reflectivity field for a SGP cirrus. The ability (sensitivity) of the two radar systems to capture the structure of the thick cirrus layer is comparable. Since the Ka-SACR uses shorter integration times compared to the KAZR (high power Klystron transmitter compared to the low output Travelling Wave Tube), it allows comparable sensitivity performance. As expected, the KAZR observations provide a very high resolution mapping of the cirrus cloud structure (Fig. 8c). The post-processed Ka-SACR reflectivity (Fig. 8b) observations are of much lower temporal resolution (20 s vs 2 s for the KAZR). The temporal resolution of the CW-gridded Ka-SACR reflectivities (Fig. 8a) is set to 3 s in this case and provide a smoother field of radar reflectivity that compares well with the KAZR reflectivity field. A comparison of the time series of the radar reflectivity at a specific height (shown by the black line in Fig. 8c) indicates that the Ka-SACR gridded observations that are based on the Barnes interpolation scheme agree better with the KAZR high-resolution measurements (Fig. 8d).

A similar comparison of the vertical Doppler velocity field is shown for a low-level stratus cloud observed at TCAP (Fig. 9). This comparison is more challenging since boundary layer clouds usually have a turbulent vertical velocity field (Kollias and Albrecht, 2000). It is important to note that the Ka-SACR has a dead zone of more than 600 m due to the use of pulse compression mode to enhance its sensitivity. Thus, the Ka-SACR observations miss a part of the cloud near the cloud base that the vertically pointing WACR observed (Fig. 9c). Starting with the cloud boundaries, it is clear that both the post-processed and the gridded Ka-SACR observations capture the cloud-top height variability observed by the high resolution WACR. The WACR cloud-top height is higher, demonstrating the higher sensitivity of the WACR. The WACR Doppler velocity observations reveal a sequence of coherent updraft and downdraft structures. In this particular example, the processed Ka-SACR Doppler velocities extracted at zenith pointing (Fig. 9b) resolve the coherent dynamical structures. In general, the ability of

AMTD
6, 9579–9621, 2013

the Ka-SACR to resolve dynamical structures in boundary layer clouds will depend on the horizontal wind speed and the horizontal scale of the in-cloud vertical motions. The gridded Ka-SACR Doppler velocity field provides a smoother field (Fig. 9a). Notice, in the gridded field, that the interpolation has horizontally stretched the dynamical structures however, their magnitude is maintained and no artefacts have been introduced. This fact is reflected in the overall good agreement between the gridded field and the high-resolution WACR observations. A comparison of the time series of the Doppler velocity at a specific height (shown by the black line in Fig. 9c) confirms that the Ka-SACR gridded observations capture most of the variance of the Doppler velocity field as observed by the WACR (Fig. 9d).

4 Retrieval of vertical Doppler velocity component from radial Doppler velocity measurements

The vertical Doppler velocity ($V_{D,V}$) in clouds is the sum of the vertical air motion (w_{AIR}) and the reflectivity-weighted particle fall velocity (V_F). Depending on the relative contribution of the two terms, the $V_{D,V}$ can be used to estimate updraft mass flux, high-order vertical air motion statistics (Kollias and Albrecht, 2000), for aerosol activation studies near the cloud base and for particle size retrievals (Frisch et al., 1995; Deng and Mace, 2006). Scanning cloud radars measure the radial Doppler velocity ($V_{D,\theta}$) component that is composed of the projected horizontal wind velocity parallel to the RHI scan plane ($V_{H,RHI}$) and the projected $V_{D,V}$ as Eq. (6) depicts and as Fig. 10 illustrates.

$$V_{D,\theta}(\theta) = V_{H,RHI}\cos(\theta) + V_{D,V}\sin(\theta). \quad (6)$$

where θ is the elevation angle. At the two extreme elevation angles, vertically ($\theta = 90^\circ$) and horizontally ($\theta = 0^\circ$), the radial Doppler velocity is dominated by $V_{D,V}$ and $V_{H,RHI}$ respectively. Thus, the zenith measurements from the SACR or the collocated profiling cloud radar can serve as a reference for the order of magnitude of the vertical velocity retrievals. Adversely, as the radar beam moves away from zenith, the horizontal wind

AMTD
6, 9579–9621, 2013

contribution ($V_{H,RHI}\cos(\theta)$) increases tracing a sinusoidal pattern (Velocity–Elevation Display, VED) similar to the cosine pattern seen in the classic Velocity–Azimuth Display (Lhermitte and Atlas, 1961; Browning and Wexler, 1968). If $V_{H,RHI}$ is known with reasonable accuracy, then a best estimate of the vertical Doppler velocity component can be retrieved.

4.1 Estimation of the horizontal wind component parallel to the RHI scan plane $V_{H,RHI}$

At the ARM sites, a total of 2 to 4 soundings are launched daily to provide profiles of the thermodynamic structure of the atmosphere. However, considerable variability of the horizontal wind profile is expected between the 6–12 h gaps especially in the boundary layer. Furthermore, the retrieved quantity $V_{D,V}$ has small magnitudes in clouds, thus, it is important to have an accurate knowledge of the wind field. The magnitude of V_F varies from negligible in the case of cloud droplets, to 0.5–2.0 m s^{-1} for drizzle and ice/snow particles, up to 4.0–9.0 m s^{-1} in the case of rain (at reference surface conditions). The technique is applicable to clouds and precipitation with variable V_F since our objective is to retrieve the best estimate for $V_{D,V}$ and not to decompose $V_{D,V}$ to its components. The application of the technique is limited to cloud systems with negligible horizontal gradient of $V_{H,RHI}$ over the range of 10–20 km. In effect, it is applicable to cloud systems that do not alter the environmental wind flow in any significant way (e.g. deep convective clouds). Another limitation of the technique is the need to have hydrometeor detections at a particular height on each side of the radar and over a range of elevation angles to minimize the uncertainty in the retrieved $V_{H,RHI}$. Although 100 % hydrometeor fractional coverage is not required to retrieve a $V_{H,RHI}$, a large number of points will reduce the impact of the $V_{D,V}$ variability on the retrievals.

The input to the $V_{D,V}$ retrieval technique are the 2-D CW-gridded RHI planes. The retrievals are performed at each gridded height with hydrometeor detections and for all the 2-D gridded planes that compose a 19 min set (380 for $\Delta t = 3$ s). In principal, the technique used is similar to the VAD analysis (Browning and Wexler, 1968) with

AMTD
6, 9579–9621, 2013

a few modifications that are discussed below. First, at each constant height all $V_{D,\theta}$ observations at elevations 75–105° are averaged to produce a first estimate of the average value of $\langle V_F \rangle$. Subsequently, all $V_{D,\theta}$ observations at elevations lower than 75° or higher than 105° are used to produce estimates of $V_{H,RHI}$ at each elevation using the following formula:

$$V_{H,RHI}(\theta) = \frac{V_{D,\theta}(\theta) - \langle V_F \rangle \sin(\theta)}{\cos(\theta)} \quad (\theta < 75^\circ \text{ or } \theta > 105^\circ). \tag{7}$$

Rather than estimating the mean and the standard deviation of the $V_{H,RHI}(\theta)$, a linear model of $V_{H,RHI}(x)$ is fitted to the dataset (x, $V_{H,RHI}(x = z\tan(\theta)^{-1})$):

$$V_{H,RHI}(x) = \beta + \alpha x. \tag{8}$$

The intercept ($\beta, \mathrm{m\,s^{-1}}$) represents the bulk of $V_{H,RHI}$ and the slope ($\alpha, \mathrm{s^{-1}}$) is introduced to quantify small linear trends. The estimation of a linear fit rather than the direct estimation of the mean is based on the analysis of a large dataset of Ka-SACR CW-RHI observations that have demonstrated the presence of small horizontal wind variations across the Ka-SACR scan plane. Considering that several of the SACR systems are mobile, the use of the linear fit is appropriate to account for horizontal wind variations related to topographic influences, sea-land contrast, etc. The parameters α and β are estimated at each gridded height and for each range-height planes. The smoothness of the field of the parameters α and β is used to evaluate the robustness of the proposed technique.

Subsequently, Eq. (6) is used to retrieve the best estimate of the vertical Doppler velocity at each height and for each range-height planes. Figure 11 shows two examples of processed Ka-SACR Doppler velocities and the corresponding retrieved vertical Doppler velocities. The stratus cloud observations were recorded at TCAP and the cirrus cloud observations were recorded at the SGP. It is apparent that the processed Doppler velocity fields (Fig. 11a and c) are of little scientific use in the raw

AMTD
6, 9579–9621, 2013

format. Their values depend on the combination of the atmospheric wind profile and the Ka-SACR azimuth and elevation angle. The retrieved vertical Doppler velocity fields (Fig. 11b and d) are not influenced by the two aforementioned factors, thus, more related to vertical dynamics and particle sedimentation. In the case of the stratus cloud, there is no drizzle thus the observed vertical Doppler velocity structures are manifestations of vertical air motion drafts. In the cirrus case, particle sedimentation (V_F) is non-negligible. The retrieved vertical Doppler velocity field is a combination of vertical dynamics (e.g., gravity waves) and particle sedimentation. In both cases, the retrievals are noisy near cloud edges due to the reduced amount of cloud observations available to estimate wind speed.

4.2 Evaluation of the 3-D vertical Doppler velocity retrievals

At each height and range, the mean of different Doppler velocity components in time is computed (19 min average). Examples of a stratus case and a cirrus are presented in Fig. 12a and Fig. 12b respectively. The observed (post-processed) Ka-SACR Doppler velocities, at the middle of the cloud layer (constant height) ($V_{D,\theta}$ red lines) and the fit ($V_{H,RHI}\cos(\theta)$, blue lines) and its offset $\langle V_F \rangle$ are shown for each case. As expected, $\langle V_F \rangle$ is negligible in the stratus and 0.3 m s^{-1} in the cirrus. The temporally averaged retrieved vertical velocity component and its variance (solid and dashed black lines) are a good indicator of the quality of the retrieved field at each height and range for all times and can be used as a quality flag for the retrieved vertical Doppler velocity field. Normally, the standard deviation of vertical Doppler velocity measurements is an indicator of in-cloud turbulence intensity. In the case of the stratus layer, the standard deviation is almost constant within ±1.5 km along scan range from the radar. Beyond this range, the standard deviation grows fast. Since there is no apparent reason for the cloud to be more turbulent at far ranges, it is plausible to assume that the observed growth in the standard deviation is due to erroneous estimates of $V_{D,V}$ at far ranges. In the case of the cirrus layer the retrievals are stable up to much larger ranges (±10 km). This

AMTD
6, 9579–9621, 2013

difference is due to the fact that at higher heights, larger ranges can be covered with the same elevation angle swath. Note that the enhancement of the vertical Doppler velocity standard deviation for positive range values ($x > +4$ km) is associated with weaker radar echoes and more areas with no radar detections in time. The estimates of $V_{D,V}$ standard deviation will be included in any future products based on the proposed gridding and retrievals technique.

Examples of the unique insights to 3-D cloud dynamics provided by the Ka-SACR gridded observations of vertical Doppler velocity are shown in Fig. 13. A ground-parallel cross-section near the middle of the clouds as well as a range-height cross-section in the middle of the scanning period (10 min) are presented. The stratus cloud layer extends for a 10 km range as shown in Fig. 13a while the cirrus cloud layer extends across a 20 km range as illustrated in Fig. 13b. The stratus cloud is characterized by very low radar reflectivity values and no echoes below the cloud base, thus the influence of drizzle particle sedimentation (V_F) to the observed $V_{D,V}$ is negligible. Given this, the $V_{D,V}$ field is representative of the vertical air motions (w_{AIR}) in the cloud layer. The gridded $V_{D,V}$ observations clearly indicate the presence of linear, coherent dynamical structures (positive: updrafts, negative: downdrafts) with vertical extend from cloud base to cloud top. Those features also transit faultlessly from positive to negative crosswind ranges which validates that the component of the horizontal wind has been successfully removed. In the deep cirrus layer, particle sedimentation (V_F) is not negligible and results to overall negative $V_{D,V}$ values with comparable velocities across range further supporting the successful removal of the horizontal wind contribution. The horizontal plane of $V_{D,V}$ shows low frequency variability that can be the result of the action of gravity waves combined with spatial inhomogeneity in particle sedimentation. The vertical cross section indicates a complicated vertical structure with several vertical layers with different fall velocities.

AMTD
6, 9579–9621, 2013

5 Summary

Scanning cloud radars are currently operational at several ground-based supersites around the world. Their observations aim to address the need to: (i) describe the 3-D cloudy atmosphere (morphology and dynamics) and (ii) to track and monitor the lifetime of clouds. The Cross-Wind Range Height Indicator (CW-RHI), a sequence of scans that slice cloud layers that move over the radar site in a plane perpendicular to that of the cloud layer mean wind direction, is a sampling strategy often used for cloud radars.

Independent of the scan strategy operated, it is apparent that radar-derived cloud fraction CF_{Hor} and 3-D hydrometeor boundaries depend on the radar sensitivity that decreases with the square of the range from the radar. Using profiling radar observations from marine boundary layer clouds, the dependency of the measured CF_{Hor} on radar sensitivity is demonstrated. In non-drizzling clouds, a drop of the radar sensitivity from −30 to −20 dBZ can result in a dramatic change in the radar-derived CF_{Hor}. Similar analyses at different ARM sites and for different cloud systems can be used to: (i) assess the low CF_{Hor} bias introduced with range and (ii) to identify a radar reflectivity threshold dBZ_{thres} (i.e., before we reach the radar sensitivity regime where $\partial CF_{Hor}/\partial dBZ$ is large) that is sufficient to observe the bulk of the cloud structure of interest. Since, the selection of a radar reflectivity threshold also determines the maximum range this sensitivity can achieve, this approach could lead to variable domains of 3-D gridded products. Different products could also lead to different 3-D gridded domains. For example, if we want to map 3-D drizzle structures, a large gridding domain is possible. It is also conceivable that if a particular radar reflectivity is selected for a particular domain, then all radar reflectivities below the threshold values are removed to generate a radar-range independent 3-D gridded product.

The suitability of a CW-RHI to addresses the need to describe the 3-D cloudy atmosphere is evaluated here. The Ka-SACR observations are initial post-processed in their native polar coordinate system to: (i) detect hydrometeors, (ii) correct for gaseous attenuation, (iii) remove Doppler velocity folding and (iv) filter out insect echoes in the

AMTD
6, 9579–9621, 2013

boundary layer. Subsequently, all CW-RHI polar coordinate radar observations (one horizon-to-horizon scan) are gridded to a 2-D Cartesian grid. The gridding algorithm accounts for the 2-D beam geometry and identifies for each grid point all radar observations within its neighborhood. Then, all 2-D gridded radar observations are gridded along the time dimension. The grid domain size and the grid spacing are user depended. Four different gridding methods are available: maximum value, mean value, Cressman and Barnes. The Cressman, Barnes and mean value schemes produce very similar results. The possibility of a hybrid scheme that uses Cressman or Barnes everywhere but near the cloud edges is considered. Near cloud edges, the maximum value interpolation method performs best since the quality of the radar observables strongly depend on signal-to-noise conditions.

Another important aspect that is evaluated here is the ability of the current CW-RHI scan strategy to resolve the 3-D morphological (i.e., as depicted by the radar reflectivity) and dynamical (i.e., as depicted by the Doppler velocity) structure of layer clouds. Comparisons of the time-height composite generated by extracting the vertically pointing beams of the Ka-SACR with the time-height composites from the dedicated profiling cloud radars at the ARM sites clearly indicates that although we are scanning from horizon-to-horizon with a relatively slow antenna scan rate (9° per second), the Ka-SACR is able to resolve all important structures.

Gridded radar reflectivity fields can be used to study 3-D cloud inhomogeneity. However, off-nadir radar Doppler measurements critically depend on the projection of the horizontal wind to the radar line-of-sight. Thus, the observed Ka-SACR Doppler velocities are decomposed into the contribution of the projected-to-the-scan plane horizontal wind and vertical Doppler velocity. The decomposition technique is applied to the 3-D gridded Doppler range-height velocity fields independently. At each height independently, the Doppler velocity measurements at elevation angles 30° to 75° and 105° to 150° are used to estimate $V_{H,RHI}$ and its gradient (if any) along the scan plane, while the Doppler measurements at elevation angles 75° to 105° are used to estimate the mean Doppler velocity offset due to particle sedimentation. Finally, the contribution of the

AMTD
6, 9579–9621, 2013

horizontal wind $V_{H,RHI}$ is removed and the residual Doppler velocities are corrected for radar centricity (divided with the sine of the elevation angle) to retrieve a best estimate of the vertical Doppler velocity component.

Analysis of the standard deviation of the retrieved 3-D $V_{D,V}$ field suggests that the retrievals of $V_{D,V}$ are noisy for elevation angle lower that 60° or higher than 120°. This assessment is also supported by the comparison of the higher moments of the 3-D retrieved $V_{D,V}$ field with those derived from the profiling ARM radars (KAZR/WACR). Despite this limitation, the best estimate of the vertical Doppler velocity component provides unique information on the 3-D coherent dynamical structures in clouds. Such information cannot be obtained from profiling cloud radars and can lead to an improved understanding of cloud dynamics and their relationship to large-scale meteorology.

Appendix A

Interpolation schemes available for gridding Ka-SACR data

A1 Maximum value scheme

The value in the grid point is determined by the observational value having a maximal reflectivity among the observational values "influencing" the value at this grid point. Let N_k be the total number of observational points F^{obs} having an influence on the value F_g at grid point x_{ix}, z_{iz}, and let $d_{(i,j),k}$ be the distance between the grid point F_g and kth observational point $(x_{i,j}, z_{i,j,k})$, where $k \in (1, N_k)$. The value F_g at the grid point x_{ix}, z_{iz} is given by:

$$F_g(x_{ix}, z_{iz}) = \mathrm{Max}\left\langle F^{obs}_{(i,j),k} \right\rangle . \quad \text{(A1)}$$

AMTD
6, 9579–9621, 2013

A2 Mean value scheme

The value in the grid point is determined by averaging the subset of observational values influencing a value in a given grid point

$$F_g(x_{ix}, z_{iz}) = \frac{\sum_k^{N_k} F^{obs}_{(i,j),k}}{N_k}. \quad \text{(A2)}$$

A3 Cressman-type method

The value F_g at the grid point x_{ix}, z_{iz} is given by

$$F_g(x_{ix}, z_{iz}) = \frac{\sum_k^{N_k} w^{(ix,iz)}_{(i,j),k} F^{obs}_{(i,j),k}}{\sum_k^{N_k} w^{(ix,iz)}_{(i,j),k}} \quad \text{(A3)}$$

with the Cressman weighting function w at the grid point (x_{ix}, z_{iz}) given as:

$$w^{(ix,iz)}_{(i,j),k} = \frac{R^2_{(i,j),k} - d^2_{(i,j),(ix,iz),k}}{R^2_{(i,j),k} + d^2_{(i,j),(ix,iz),k}} \quad \text{for } d^2 \le R^2$$
$$w^{(ix,iz)}_{(i,j),k} = 0, \quad \text{for } d^2 > R^2 \quad \text{(A4)}$$

where d^2 is the distance from the center of radar resolution volume r_i, θ_j of the kth observational point, $k \in (1, N_k)$ to the grid point x_{ix}, z_{iz}. The weight of a measurement is equal to one if it is located exactly on the grid point and equal to zero on the edge of and outside the sphere with radius R.

The radius of influence $R_{(i,j),k}$ depends on the size of the radar resolution volume relative to the grid resolution, and is defined as:

$$R_{(i,j),k} = \text{Max}[R_{d1}, R_{d2}] \quad \text{(A5)}$$

AMTD
6, 9579–9621, 2013

where

$$R_{d1} = \left[\frac{\Delta x^2 + \Delta z^2}{4}\right]^{0.5}$$
$$R_{d2} = \left[\mathrm{d}r^2 + (r_i + 0.5\mathrm{d}r)^2 \sin^2(0.5\mathrm{Max}\{\theta_{j+1} - \theta_j, bw\})\right]^{0.5} \quad \text{(A6)}$$

In the standard approach, for each grid point, all observational values within the specified radius of influence are selected for application of distance depending scheme based on chosen weighting function. While large values of radius of influence increase the smoothing effects, very small values can create gaps in gridded data. Large values of radius of influence can also introduce artificial values at grid points corresponding to observational cloud-free pixels, especially near cloud boundaries. In our approach, a radius of influence is defined in such a way that its value is no larger than necessary. Obviously, the minimal value is imposed by the choice of grid resolution, and is equal to radius of a circle circumscribed around a grid box (R_{d1}). However, a size of radar resolution volume increases with increasing distance from radar, so it is necessary to increase the radius of influence to some value that would conform to the size of resolution volume (R_{d2}). With these choices of radius of influence, effect of smoothing in gridded data primarily depends on choice of grid resolution. Note that only cloud pixels are examined when selecting the observational values that "influence" the value at specific grid point. Implicit consequence of the selection method is that the discontinuity in observed data, if larger than grid resolution, is preserved. When lowering the grid resolution in x and z, the smoothing takes effect and cloud boundaries tend to spread out. Although grid spacing is a parameter defined by user, the application of high grid resolution in gridding algorithm is implicitly stipulated and advised.

AMTD
6, 9579–9621, 2013

A4 Barnes-type method

The method is similar to Cressman, except a different weighting function is used:

$$w_{(i,j),k}^{(ix,iz)} = \exp\left(-\frac{d_{(i,j),(ix,iz),k}^2}{2R_{(i,j),k}^2}\right), \quad \text{for } d^2 \le R^2$$
$$w_{(i,j),k}^{(ix,iz)} = 0, \quad \text{for } d^2 > R^2 \tag{A7}$$

The weighting function (A7) is defined as in Trapp and Doswell III (2000), with the smoothing parameter defined as two times the characteristic data spacing squared. The method is expected to produce similar results to those produced by Cressman-type method.

Acknowledgements. Support for this research was funded by the Office of Biological and Environmental Research, Environmental Sciences Division of the US Department of Energy as part of the Atmospheric Systems Research (ASR) program. We would also like to thank the entire McGill Clouds Research Group for their feedback and support.

References

Askelson, M. A.: A study of the kinematic and microphysical evolution of a supercell from first echo using polarization diversity radar, in: School of Meteorology, edited by: Boyd, E., University of Oklahoma, Norman, 73019, OK, 94, 100, 1996.

Barnes, S. L.: A technique for maximizing details in numerical weather map analysis, J. Appl. Meteorol., 3, 396–409, 1964.

Browning, K. and Wexler, R.: The determination of kinematic properties of a wind field using Doppler radar, J. Appl. Meteorol., 7, 105–113, 1968.

Clothiaux, E., Miller, M., Albrecht, B., Ackerman, T., Verlinde, J., Babb, D., Peters, R., and Syrett, W.: An evaluation of a 94-GHz radar for remote sensing of cloud properties, J. Atmos. Ocean. Tech., 12, 201–229, 1995.

AMTD
6, 9579–9621, 2013

Clothiaux, E. E., Ackerman, T. P., Mace, G. G., Moran, K. P., Marchand, R. T., Miller, M. A., and Martner, B. E.: Objective determination of cloud heights and radar reflectivities using a combination of active remote sensors at the ARM CART sites, J. Appl. Meteorol., 39, 645–665, 2000.

Cressman, G. P.: An operational objective analysis system, Mon. Weather Rev., 87, 367–374, 1959.

Davis, A., Marshak, A., Cahalan, R., and Wiscombe, W.: The Landsat scale break in stratocumulus as a three-dimensional radiative transfer effect: implications for cloud remote sensing, J. Atmos. Sci., 54, 241–260, 1997.

Deng, M. and Mace, G. G.: Cirrus microphysical properties and air motion statistics using cloud radar Doppler moments, Part I: Algorithm description, J. Appl. Meteorol. Climatol., 45, 1690–1709, 2006.

Doviak, R. J. and Zrnić, D. S.: Doppler Radar and Weather Observations, Academic Press, 1993.

Frisch, A., Fairall, C., and Snider, J.: Measurement of stratus cloud and drizzle parameters in ASTEX with a Kα-band Doppler radar and a microwave radiometer, J. Atmos. Sci., 52, 2788–2799, 1995.

Fulton, R. A.: WSR-88D polar-to-HRAP mapping, National Weather Service, Hydrologic Research Laboratory, Technical Memorandum, 9–9, 1998.

Hildebrand, P. H. and Sekhon, R. S.: Objective determination of noise level in Doppler Spectra, J. Appl. Meteorol., 13, 808–811, 1974.

Hinkelman, L. M., Stevens, B., and Evans, K. F.: A large-eddy simulation study of anisotropy in fair-weather cumulus cloud fields, J. Atmos. Sci., 62, 2155–2171, 2005.

Jorgensen, D. P., Hildebrand, P. H., and Frush, C. L.: Feasibility test of an airborne pulse-Doppler meteorological radar, J. Climate Appl. Meteorol., 22, 744–757, 1983.

Kollias, P. and Albrecht, B.: The turbulence structure in a continental stratocumulus cloud from millimeter-wavelength radar observations, J. Atmos. Sci., 57, 2417–2434, 2000.

Kollias, P., Clothiaux, E., Miller, M., Albrecht, B., G. Stephens and Ackerman, T.: Millimeter-wavelength radars: new frontier in atmospheric cloud and precipitation research, B. Am. Meteorol. Soc., 88, 1608–1624, 2007.

Kollias, P., Bharadwaj, N., Widener, K., Jo, I., and Johnson, K.: Scanning ARM cloud radars – Part I: Operational sampling strategies, J. Atmos. Ocean. Tech., accepted, 2013a.

AMTD
6, 9579–9621, 2013

Kollias, P., Jo, I., Borque, P., Tatarevic, A., Lamer, K., Bharadwaj, N., Widener, K., Johnson, K., and Clothiaux, E.: Scanning ARM cloud radars – Part II: Data quality control and processing, J. Atmos. Ocean. Tech., accepted, 2013b.

Lhermitte, R. M. and Atlas, D.: Precipitation motion by pulse Doppler radar, in: Proc. Ninth Weather Radar Conf, 218–223, Amer. Meteor. Soc., Boston, M A., 1961.

Mather, J. H. and Voyles, J. W.: The ARM climate research facility: a review of structure and capabilities, B. Am. Meteorol. Soc., 94, 377–392, 2013.

Miller, J. L., Mohr, C. G., and Weinheimer, A. J.: The simple rectification to Cartesian space of folded radial velocities from Doppler radar sampling, J. Atmos. Ocean. Tech., 3, 162–174, 1986.

Mohr, C. and Vaughan, R.: An economical procedure for Cartesian interpolation and display of reflectivity factor data in three-dimensional space, J. Appl. Meteorol., 18, 661–670, 1979.

Qian, Y., Long, C. N., Wang, H., Comstock, J. M., McFarlane, S. A., and Xie, S.: Evaluation of cloud fraction and its radiative effect simulated by IPCC AR4 global models against ARM surface observations, Atmos. Chem. Phys., 12, 1785–1810, doi:10.5194/acp-12-1785-2012, 2012.

Randall, D. A., Xu, K.-M., Somerville, R. J., and Iacobellis, S.: Single-column models and cloud ensemble models as links between observations and climate models, J. Climate, 9, 1683–1697, 1996.

Rémillard, J., Kollias, P., Luke, E., and Wood, R.: Marine boundary layer cloud observations in the Azores, J. Climate, 25, 7381–7398, 2012.

Rosenkranz, P. W.: Water vapor microwave continuum absorption: a comparison of measurements and models, Radio Sci., 33, 919–928, 1998.

Shupe, M. D., Walden, V. P., Eloranta, E., Uttal, T., Campbell, J. R., Starkweather, S. M., and Shiobara, M.: Clouds at Arctic atmospheric observatories, Part I: Occurrence and macrophysical properties, J. Appl. Meteorol. Climatol., 50, 626–644, 2011.

Somerville, R. and Iacobellis, S.: Single-column models, ARM observations, and GCM cloud-radiation schemes, Phys. Chem. Earth, 24, 733–740, 1999.

Stokes, G. M. and Schwartz, S. E.: The Atmospheric Radiation Measurement (ARM) program: programmatic background and design of the cloud and radiation test bed, B. Am. Meteorol. Soc., 75, 1201–1221, 1994.

Trapp, R. J. and Doswell III, C. A.: Radar data objective analysis, J. Atmos. Ocean. Tech., 17, 105–120, 2000.

AMTD
6, 9579–9621, 2013

Zhang, J., Howard, K., and Gourley, J.: Constructing three-dimensional multiple-radar reflectivity mosaics: examples of convective storms and stratiform rain echoes, J. Atmos. Ocean. Tech., 22, 30–42, 2005.

Zinner, T. and Mayer, B.: Remote sensing of stratocumulus clouds: uncertainties and biases due to inhomogeneity, J. Geophys. Res., 111, D14209, doi:10.1029/2005JD006955, 2006.

AMTD

6, 9579–9621, 2013

Table 1. Specification of radars used in this study: Ka-band ARM Zenith Radar (KAZR), W-band ARM Cloud Radar (WACR), Ka-band Scanning ARM Cloud Radar (Ka-SACR). Transmitter types: traveling-wave tube amplifier (TWTA) and extended interaction klystron amplifier (EIKA).

Parameters	KAZR	WACR	Ka-SACR
Transmitter type	TWTA	EIKA	EIKA
Peak power output (W)	150	1600	2200
Duty Cycle (%)	25.0	1.0	5.0
Center frequency (GHz)	34.86	95.00	35.29
Antenna size (m)	3.0	1.22	1.82
3-dB beamwidth (°)	0.19	0.18	0.33
Range resolution (m)	30	43	30
Temporal resolution (s)	2	2	0.04
Nyquist Velocity ($m\,s^{-1}$)	5.95	8.0	10.53
Integration time (s)	2	2	0.037
Sensitivity (dBZ)*	−50	−50	−50

* Accounting for signal integration time, at 1 km.

AMTD
6, 9579–9621, 2013

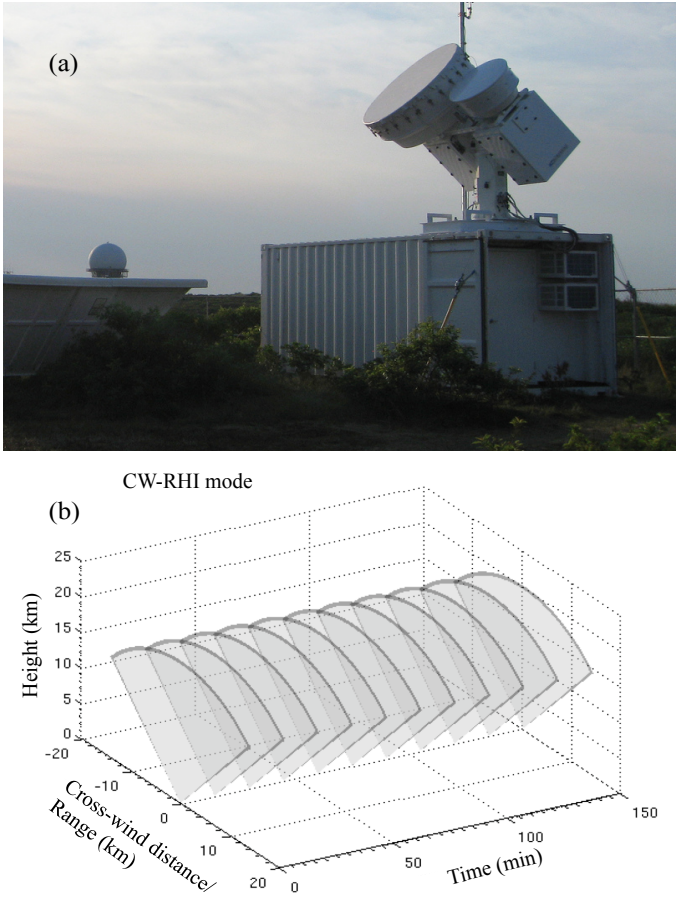

Fig. 1. (a) The Ka/W-SACR at Cape Cod during the AMF deployment. A similar system is deployed at the ARM SGP site, **(b)** Schematic of the CW-RHI scan strategy.

AMTD
6, 9579–9621, 2013

Evaluation of gridded SACR reflectivity and velocity retrievals

K. Lamer et al.

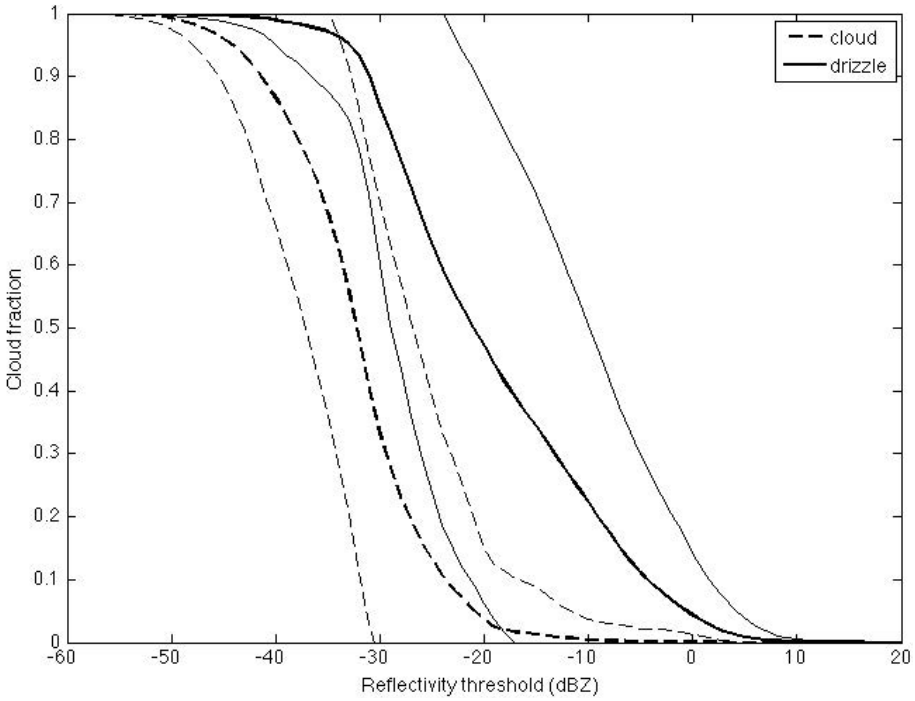

Fig. 2. The radar-detected cloud fraction (mean (thick lines) and standard deviation (thin lines)) for boundary layer clouds at the Azores during the CAP-MBL deployment as a function of the radar sensitivity (threshold). Two categories of boundary layer clouds are shown: drizzle-free clouds (dashed lines) and drizzling clouds (solid lines).

AMTD
6, 9579–9621, 2013

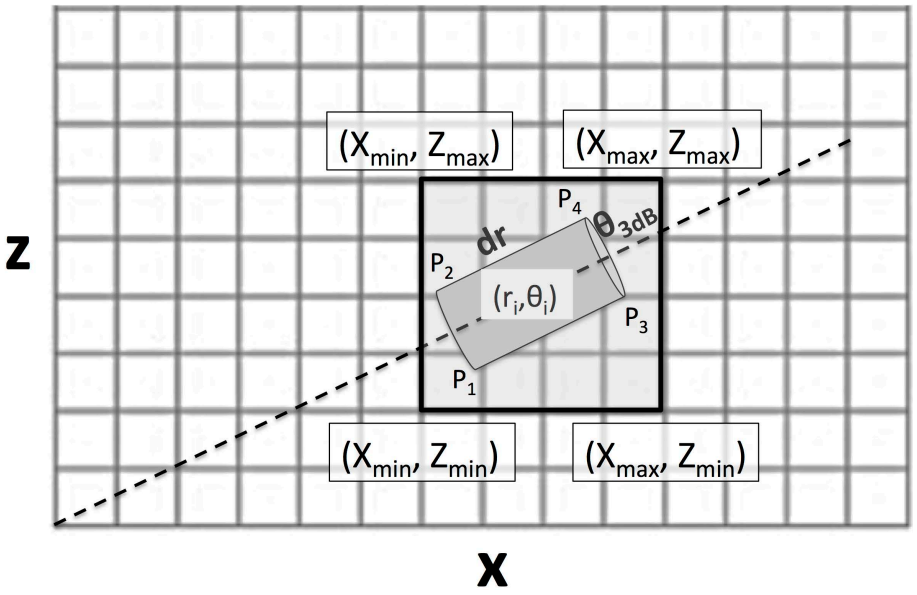

Fig. 3. Vertical cross section of radar resolution volume with fixed azimuth. Identified are: the beam width ($\theta_{3\,\mathrm{dB}}$), the pulse length (dr), the center of the radar volume in polar coordinates (r_i, θ_j), the edges of radar volume in polar coordinates (P_{1-4}) and the smaller rectangle defined on the Cartesian grid that includes the radar resolution area ($X_{\mathrm{min/max}}$, $Z_{\mathrm{min/max}}$).

AMTD
6, 9579–9621, 2013

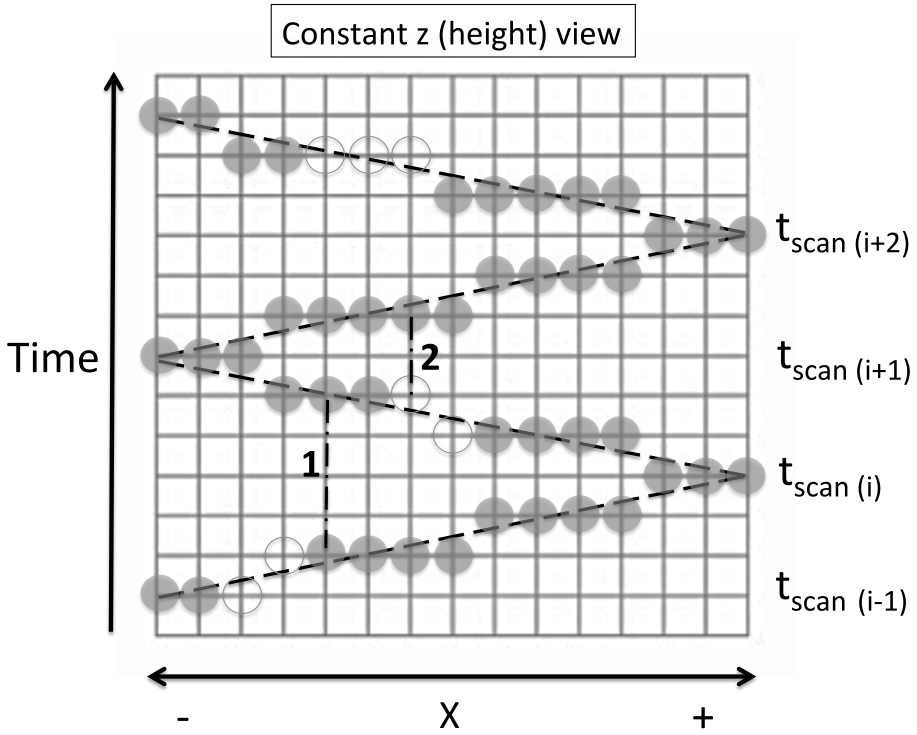

Fig. 4. Schematic of the consecutive CW-RHI scans at constant height. Scenario 1: neighboring scans contain cloud (dark shaded circles). Scenario 2: previous scan does not contain cloud (empty circles) and the next scan contains cloud.

AMTD
6, 9579–9621, 2013

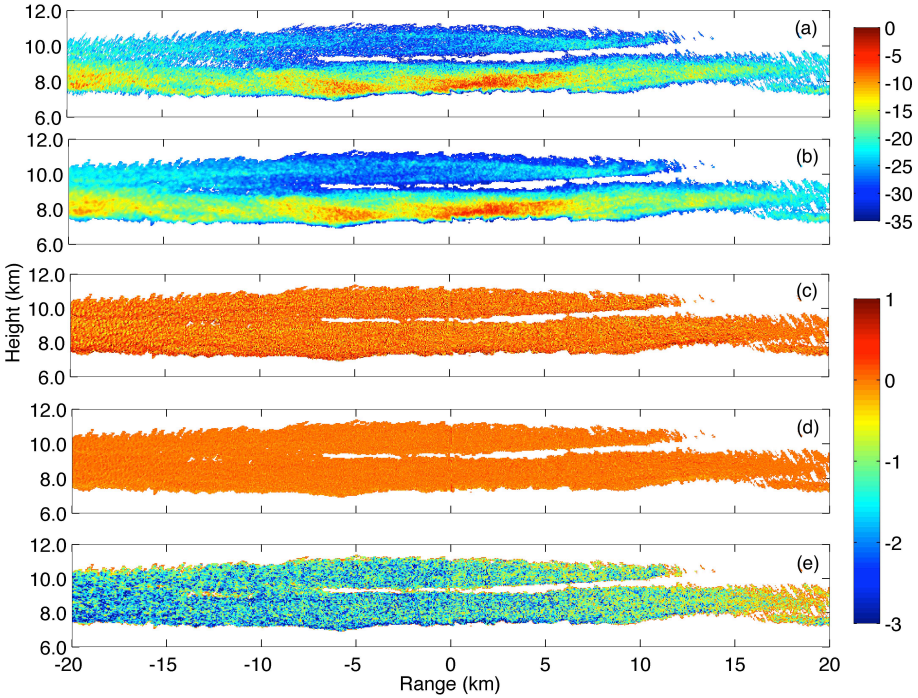

Fig. 5. Ka-SACR radar reflectivity 2-D gridding ($\Delta x = 50$ m, $\Delta z = 50$ m) for a thick cirrus cloud observed at the ARM SGP site: **(a)** polar coordinates (r,θ) Ka-SACR post-processed data, **(b)** x-z gridded radar reflectivity using the Barnes scheme, **(c)** difference in gridded radar reflectivity between the Barnes and Cressman schemes ($dBZ_{BARNES} - dBZ_{CRESSMAN}$), **(d)** difference in gridded radar reflectivity between the Barnes and Mean value schemes, and **(e)** difference in gridded radar reflectivity between the Barnes and Maximum value schemes.

AMTD
6, 9579–9621, 2013

Evaluation of gridded SACR reflectivity and velocity retrievals

K. Lamer et al.

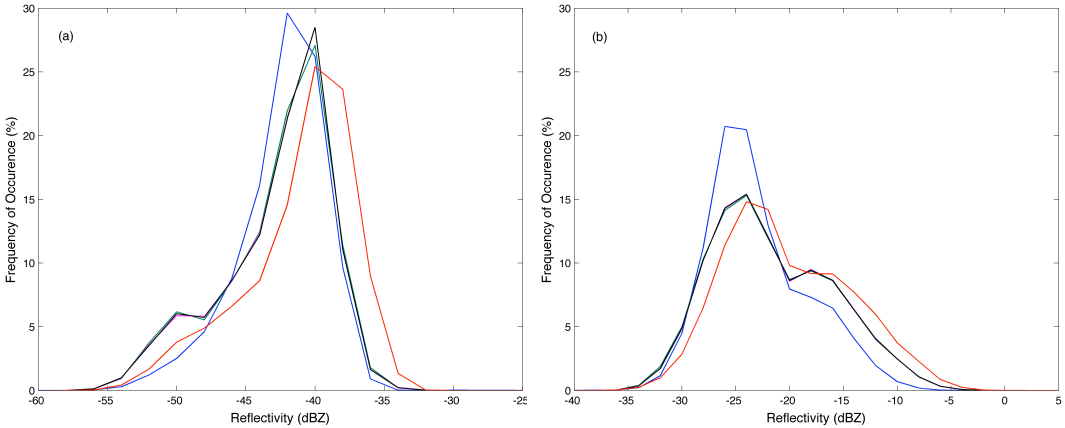

Fig. 6. Area distribution histograms of Ka-SACR radar reflectivity 2-D gridding for a **(a)** stratus cloud ($\Delta x = 25\,\mathrm{m},\ \Delta z = 25\,\mathrm{m}$) and a **(b)** cirrus cloud ($\Delta x = 50\,\mathrm{m},\ \Delta z = 50\,\mathrm{m}$). The radar reflectivitiy histograms are shown for the polar coordinates (r, θ) Ka-SACR post-processed data (blue) and for all interpolation schemes (Cressman: green, Barnes: black, Maximum: red and Mean: magenta).

AMTD
6, 9579–9621, 2013

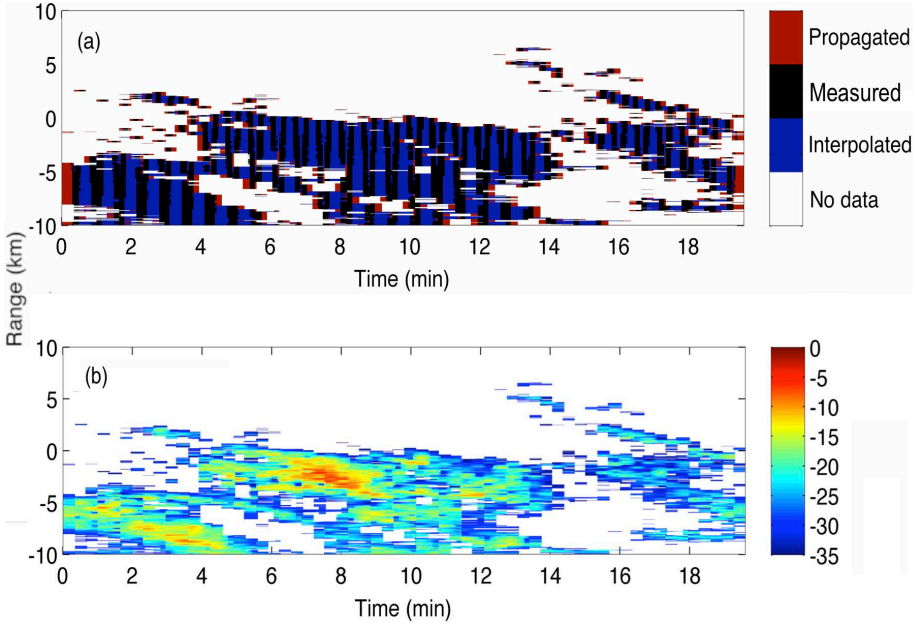

Fig. 7. Ground-parallel cross-section (constant height) and x-axis along the scanning direction of a cirrus cloud observed at SGP **(a)** the cloud mask of the 3-D gridded data, and **(b)** the 3-D gridded Ka-SACR radar reflectivity field.

AMTD
6, 9579–9621, 2013

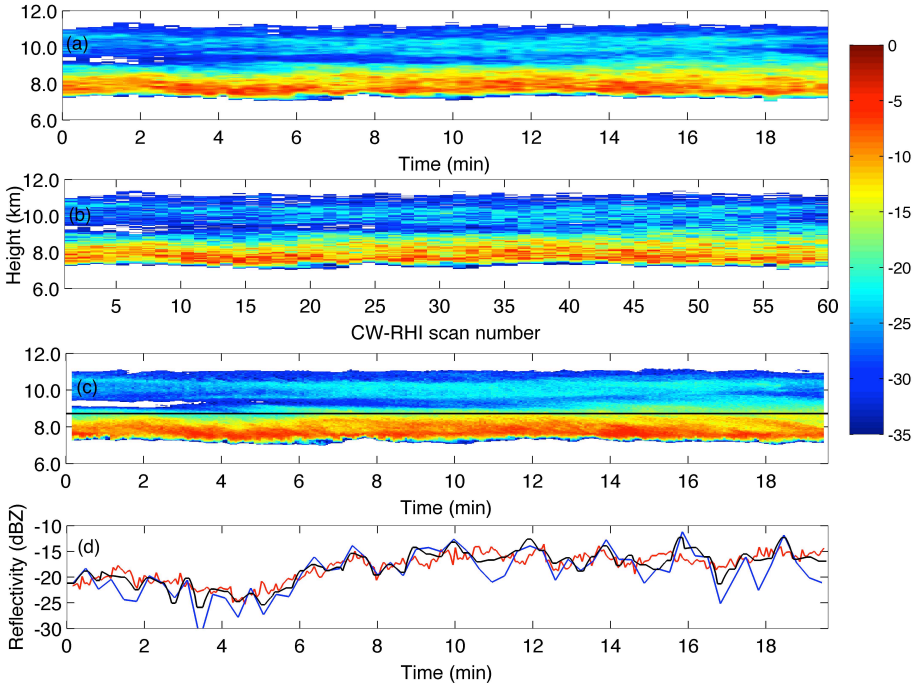

Fig. 8. Time-height radar reflectivity field of a cirrus observed at SGP with the **(a)** Ka-SACR gridded ($x = 0$ m), **(b)** Ka-SACR post-processed polar coordinates ($\theta = 0^{\circ}$), **(c)** profiling KAZR. The black line indicates the height of panel d retrievals. **(d)** Time series of radar reflectivity from Ka-SACR gridded ($x = 0$ m, black), Ka-SACR post-processed polar coordinates ($\theta = 0^{\circ}$, blue) and profiling KAZR (red).

AMTD
6, 9579–9621, 2013

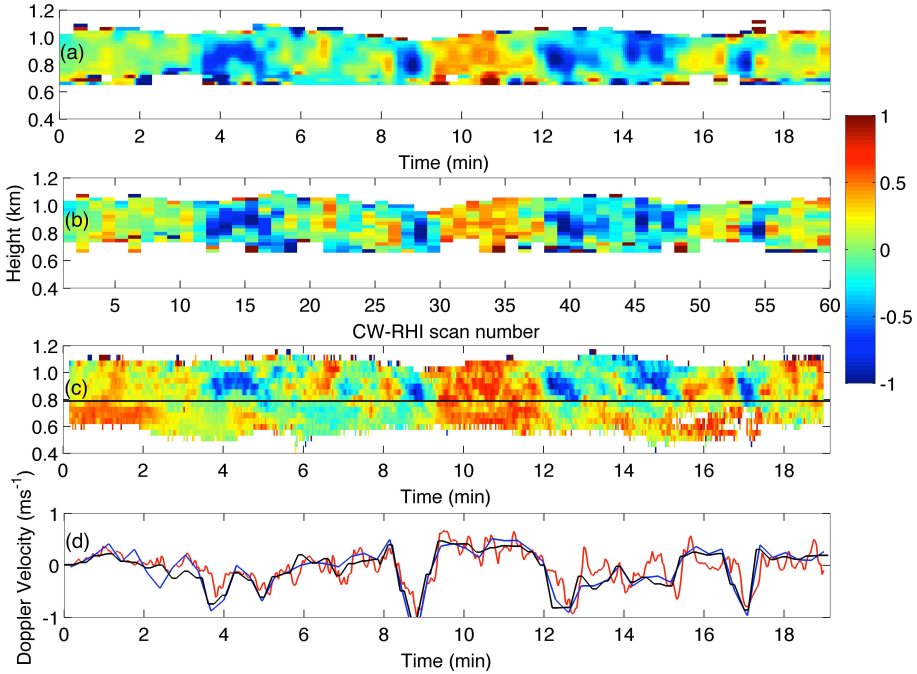

Fig. 9. Time-height radar Doppler velocity field of a stratocumulus observed at TCAP with the **(a)** Ka-SACR gridded ($x = 0$ m), **(b)** Ka-SACR post-processed polar coordinates ($\theta = 0^{\circ}$), **(c)** profiling KAZR. The black line indicates the height of panel d retrievals. **(d)** Time series of radar reflectivity from Ka-SACR gridded ($x = 0$ m, black), Ka-SACR post-processed polar coordinates ($\theta = 0^{\circ}$, blue) and profiling KAZR (red).

AMTD
6, 9579–9621, 2013

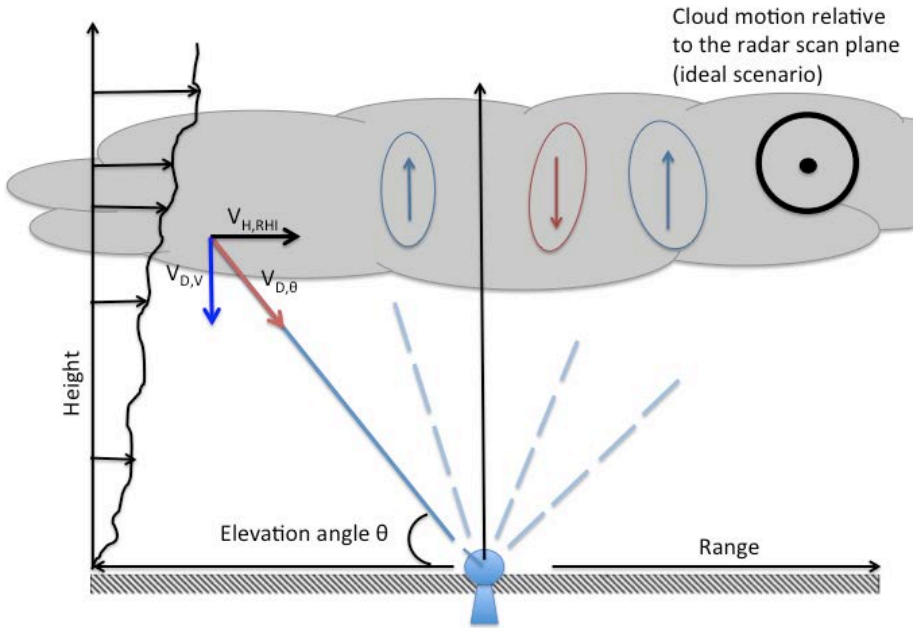

Fig. 10. Schematic of Ka-SACR CW-RHI Doppler velocity observations. Identified are: the elevation angle (θ), the horizontal wind projection on the radar scan plane ($V_{H,RHI}$), the vertical Doppler velocity ($V_{D,V}$) and the observed angular Doppler velocity ($V_{D,\theta}$).

AMTD
6, 9579–9621, 2013

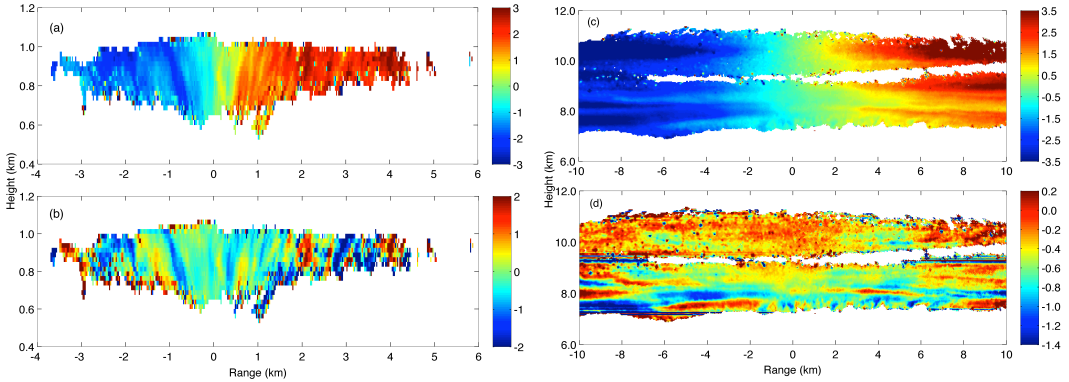

Fig. 11. 3-D gridded Ka-SACR Doppler velocity RHI planes of a stratocumulus during TCAP: **(a)** observed radial Doppler velocity and **(b)** retrieved vertical Doppler velocity compo- nent; 3-D gridded Ka-SACR Doppler velocity RHI planes of a cirrus during SGP: **(c)** observed radial Doppler velocity and **(d)** retrieved vertical Doppler velocity component.

AMTD
6, 9579–9621, 2013

Evaluation of gridded SACR reflectivity and velocity retrievals

K. Lamer et al.

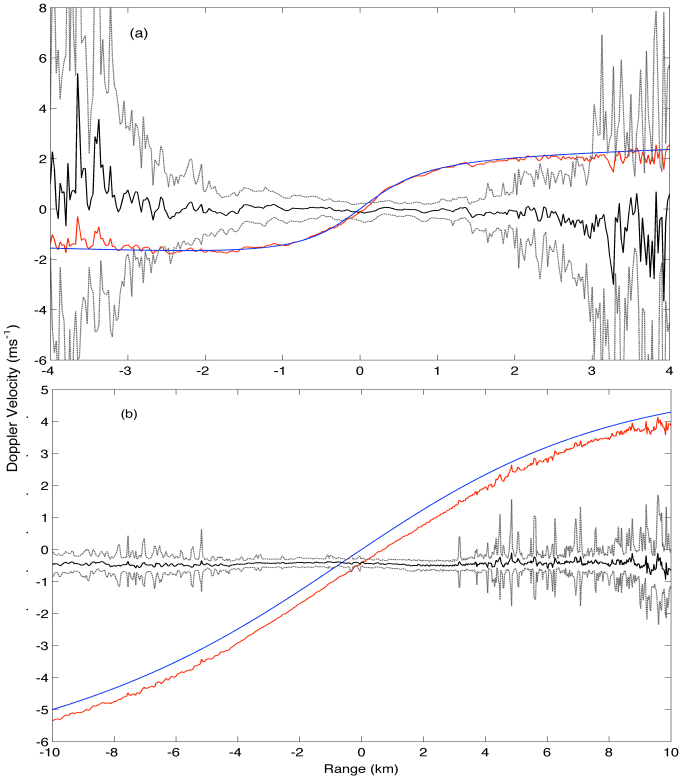

Fig. 12. Nineteen min averaged Doppler velocities at the middle of: **(a)** a stratocumulus cloud layer and **(b)** a cirrus cloud case as a function of range from the radar. The 19 min average implies that all 3-D gridded CW-RHI planes at this height have been used to estimate the mean and variance of the retrieved Doppler velocities. The radial observed Doppler velocities $V_{D,\theta}$ are shown in red, the fitted projected horizontal wind contribution ($V_{\mathrm{H,RHI}}$) the retrieved vertical Doppler velocity ($V_{D,\theta}$) in black. The standard deviation of the retrieved vertical Doppler velocity is in dashed grey.

AMTD
6, 9579–9621, 2013

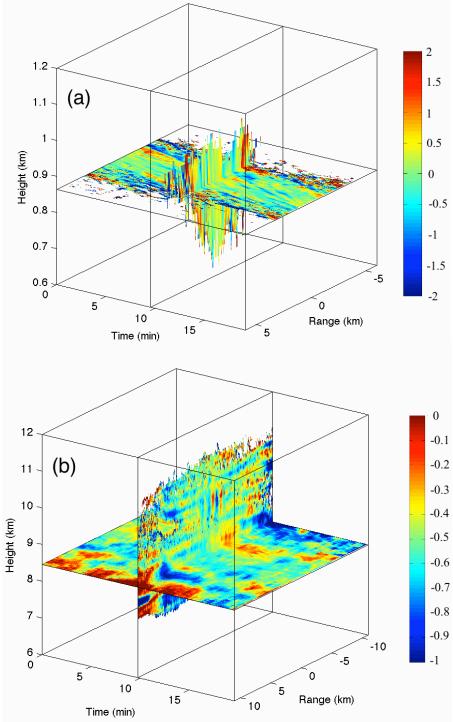

Fig. 13. 3-D representation of the retrieved vertical Doppler velocities from a set of CWRHI scans for **(a)** a stratocumulus case and **(b)** a cirrus case. The horizontal cross section is near the middle of the cloud layer and the vertical section half way through the set.

AMTD
6, 9579–9621, 2013